



Cite this: *Phys. Chem. Chem. Phys.*,
2017, 19, 6105

Correlation of the structural information obtained for europium-chelate ensembles from gas-phase photoluminescence and ion-mobility spectroscopy with density-functional computations and ligand-field theory†

Jean-François Greisch,^{‡*a} Jiří Chmela,^{‡b} Michael E. Harding,^{‡*a} Dirk Wunderlich,^{*c} Bernhard Schäfer,^a Mario Ruben,^{ad} Wim Klopper,^{ab} Detlef Schooss^{ab} and Manfred M. Kappes^{ab}

We report a combined investigation of europium(III)9-oxo-phenalen-1-one (PLN) coordination complexes, [Eu(PLN)₄AE]⁺ with AE = Mg, Ca, and Sr, using gas-phase photoluminescence, trapped ion-mobility spectrometry and density-functional computations. In order to sort out the structural impact of the alkali earth dications on the photoluminescence spectra, the experimental data are compared to the predicted ligand-field splittings as well as to the collision cross-sections for different isomers of [Eu(PLN)₄AE]⁺. The best fitting interpretation is that one isomer family predominantly contributes to the recorded luminescence. The present work demonstrates the complexity of the coordination patterns of multicenter lanthanoid chelates involved in dynamical equilibria and the pertinence of using isolation techniques to elucidate their photophysical properties.

Received 4th July 2016,
Accepted 27th January 2017

DOI: 10.1039/c6cp04656h

rsc.li/pccp

Introduction

Lanthanoids can be found in optical materials, lasers, glasses, and molecular assays. In most cases, the related applications involve photoluminescence and rely on the efficient population of the emitting levels *via* an energy transfer from one or more ligands, the so-called sensitization.^{1–4} In addition, lanthanoids can also be used as structural probes: in NMR, for example, lanthanoid shift reagents have been used for the spectral simplification and interpretation of molecules possessing various functional groups, and for the determination of enantiomeric purity.^{5–7}

The ligand-field splitting of lanthanoid levels can be monitored *via* their luminescence, which allows probing the local structure of their binding sites. This is particularly relevant for calcium binding species since europium (and other lanthanoids) can serve as calcium analogues.⁸ For example, europium complexation by gramicidin A, in a water–methanol mixture, has been shown to lead to direct f–f absorption lines consistent with two specific binding sites, one of C_{3v} symmetry, thereby restricting the number of possible ion-gramicidin conformers.⁹

In this work, we further pursue our gas-phase investigation of the intrinsic properties of photoluminescent lanthanoid complexes using mass spectrometric techniques.^{4,10,11} Inherent to the present approach is the knowledge of the gas phase of the compound's exact stoichiometry, often not known or regulated by equilibria in solution. Structural information is also obtained using trapped ion mobility spectrometry^{12–14} thereby providing additional insight into the gas-phase photoluminescence of europium complexes.

The heterodimetallic complexes^{15,16} [Eu(PLN)₄AE]⁺ with AE = Mg, Ca, and Sr studied here involve a Eu(III) ion and an alkaline earth dication bridged by deprotonated 9-hydroxyphenalen-1-one (PLN, see Fig. 1). β-Diketonates, such as PLN, are among the most important ligands for applications involving lanthanoids emitting in the visible range due to the ability of diketonates to combine a high absorption cross-section in the

^a Institute of Nanotechnology, Karlsruhe Institute of Technology (KIT),
Hermann-von-Helmholtz-Platz 1, 76344 Eggenstein-Leopoldshafen, Germany.
E-mail: jean-francois.greisch@kit.edu, michael.harding@kit.edu

^b Institute of Physical Chemistry, Karlsruhe Institute of Technology (KIT),
Fritz-Haber-Weg 2, 76131 Karlsruhe, Germany

^c Bruker Daltonik GmbH, Fahrenheitstraße 4, 28359 Bremen, Germany.
E-mail: dirk.wunderlich@bruker.com

^d Institut de Physique et Chimie des Matériaux de Strasbourg (IPCMS),
CNRS-Université de Strasbourg, Rue du Loess 23, BP 43,
67034 Strasbourg Cedex 2, France

† Electronic supplementary information (ESI) available: Synthesis description. Experimental setup description. Density-functional and ligand-field computations. Symmetry assessment using the shape factor. Structures in XYZ format. See DOI: 10.1039/c6cp04656h

‡ These authors contributed equally.

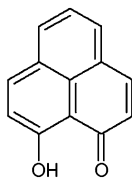


Fig. 1 Sketch of a protonated 9-oxo-phenalen-1-one (H-PLN) ligand.

near-UV or visible range with efficient sensitization of Eu(III), Tb(III), Sm(III), and Dy(III).^{17,18}

The photoluminescence spectra of Eu(III) complexes are typically dominated by transitions from the ⁵D to the ⁷F manifolds. Both manifolds are split by spin-orbit coupling into ^{2S+1}L_J multiplets: seven for the ⁷F ground state manifold and five for the ⁵D manifold. All the ^{2S+1}L_J multiplets with *J* ≠ 0 are liable to further splitting into 2*J* + 1 Stark levels due to the electrostatic field generated by the ligands.^{1,19–21} While electron repulsion and spin-orbit coupling within the f-shell induce splittings on the order of several thousand wavenumbers, the ligand-field splitting is typically less than a few hundred wavenumbers mainly due to the shielding of the Eu(III) 4f-electrons by completely filled outerlying electron shells. The most intense radiative transition occurs between the ⁵D₀ and the ⁷F₂ levels, which corresponds to approximately 16 200 cm⁻¹ (≈ 615 nm) photons. This “hypersensitive” transition is particularly sensitive to the ligand field and vanishes when the Eu(III) site possesses a center of inversion or is of *D*_{4d} symmetry,²² making it a highly suitable probe for the structural investigation of Eu(III) (or analogous metal ion) binding pockets.^{1,20} Typical coordination numbers for Eu(III) are eight or nine.^{23,24} The species studied in the present work involve six-fold coordinated Eu(III) ions and can therefore be seen as coordinatively unsaturated due to the absence of solvent molecules under gas-phase conditions.²⁵

The present work is part of a series^{4,10,11} in which we attempt to tune the properties of Eu(III) complexes having PLN as common structuring and energy-harvesting ligands by allowing them to interact with a range of small “spectator” cations. The scope of the present paper is twofold: (i) assess the sensitivity of lanthanoid luminescence towards structural changes induced by alkaline earth ions *via* the combination of photoluminescence measurements with ligand-field theory, and (ii) illustrate the importance of identifying the isomers and resolving the complexity of europium coordination patterns using high resolution trapped ion mobility. The ⁵D₀ → ⁷F_J transitions are analyzed and their splittings are tentatively correlated to structures identified using trapped ion mobility *via* the determination of the corresponding Stark levels using a combination of density-functional computations and ligand-field theory.

Experimental and computational methods

Sample preparation

The alkaline earth complexes are formed either by adding minute volumes of saturated DMSO solutions of iodide/chloride salts

of alkaline earth metals to an approximately 10⁻⁴ M solution of K[Eu(PLN)₄] whose synthesis is described in ref. 4, or by direct synthesis using Mg(OH)₂ and Ca(OH)₂ in the case of Mg[Eu(PLN)₄]₂ and Ca[Eu(PLN)₄]₂ as described in the ESI.† It is noteworthy that both approaches yield the same gas-phase data.

Trapped ion mobility spectroscopy

The ion mobility measurements were carried out at room temperature on a timsTOF instrument, *i.e.* a trapped ion mobility (TIMS) time-of-flight mass spectrometer combination (Bruker, Bremen, Germany) using nitrogen as a carrier gas. Briefly, the ions of interest were generated in an orthogonal electrospray source, transferred into the instrument *via* a glass capillary, and deflected into the entrance funnel before being focused into the TIMS cell where the carrier gas (gas flow velocity defined by the pressure difference between the entrance funnel, 2.56 mbar, and the exit funnel, 0.923 mbar) and a counteracting electric field (entrance voltage of 240 V and exit voltage of 45 V) were used to hold the ions stationary according to their mobility. After an ion accumulation time of 400 μs, a change in the deflection plate potential was used to prevent further ions from entering the cell after which the stored ions were released by reducing the counteracting electric field strength. The ions exiting the TIMS cell were then focused by the exit funnel assembly into a transfer quadrupole prior to being analyzed by a time-of-flight analyzer.

The experimental mobilities of the ions sequentially released from the TIMS cell after trapping can be described by a trapping electric field window *E* ± Δ*E* value directly related to the ion mobility *K* ± Δ*K* and the velocity of the carrier gas *v*_g *via*

$$K = \frac{v_g}{E} = \frac{A}{U_{\text{release}} - U_{\text{out}}} \quad (1)$$

where *A* is a calibration constant, *U*_{release} is the voltage at which the ions are released from the TIMS cell, and *U*_{out} is the voltage applied to the tunnel exit. The calibration constant *A* is determined from previously reported mobility values reported for calibration standards.^{12–14,26}

Reduced mobility values, *K*₀ = $\frac{P}{101325} \frac{273.15}{T} K$, were converted to collision cross-sections (Ω) using the Mason–Schamp equation:

$$\Omega = \frac{(18\pi)^{\frac{1}{2}}}{16} \frac{ze}{(k_B T)^{\frac{1}{2}}} \left[\frac{1}{m_1} + \frac{1}{m_2} \right]^{\frac{1}{2}} \frac{1}{K_0 N_0} \quad (2)$$

where *ze* is the charge of the ion, *k*_B is the Boltzmann constant, *N*₀ is the number density, and *m*₁ and *m*₂ refer to the masses of the ion and bath gas, respectively. The reported mobility resolutions correspond to Ω/ΔΩ ratios determined from the position and FWHM of Gaussian fits of the features present in the TIMS distributions. The comparison of computations and structural assignment was performed *via* the scaling of the helium cross-sections computed using the trajectory method as implemented in MOBICAL^{27,28} (version provided by Matt Bush) with Eu(III) described using the same parameters as iron.²⁹ The scaling relationship, Ω_{N₂} = 53.9 + 1.110·Ω_{He}, was inferred from the comparison of the He and N₂ cross sections reported for denatured polyalanine by Bush and coworkers.³⁰

Gas-phase luminescence

The experimental setup used is similar to the one used in ref. 31. Briefly, it consists of a temperature-regulated stretched quadrupole ion trap held at 85 K in which electrosprayed ions are (i) mass-selected, (ii) thermalized by collisions with a He buffer gas held at a constant pressure of approximately 0.2 mbar during photoexcitation, and (iii) photoexcited by the focused 458 nm line of a continuous wave (cw) Ar⁺-laser (Spectra Physics 2080-15S) orthogonal to the ion trap axis. The photoluminescence of ensembles of about 10⁴ trapped ions is recorded with no or negligible fragmentation upon photoexcitation. The ion luminescence is collected perpendicular to the excitation beam by a microscope objective (Zeiss EC PlanNeofluor 5×/0.15) through a 3 mm diameter aperture in one of the end caps. The collected light passes through a long-pass edge filter (Semrock) that removes scattered excitation light, before being focused into a fiber and sent to a spectrograph (SpectraPro 300i, Acton Research, Roper Scientific/Triax 190, Jobin-Yvon, Horiba) equipped with a CCD camera (Idus DV401A-BV, Andor/Newton EMCCD A-DU-970N-BV, Andor). The spectral resolutions of both the spectrograph and camera combinations used were 0.7 and 2.4 nm, respectively.

Density-functional computations

Neither crystal nor NMR structures exist for the species investigated in the present work. Candidate structures for the europium complexes were therefore systematically generated at the semi-empirical PM7-SPARKLE level³² using openMopac.^{33,34} Following this first step, the structures were reoptimized and the electron densities used for population analysis were calculated using DFT employing the B-P functional³⁵ in combination with the def2-TZVPP basis set^{36–38} as implemented in the TURBOMOLE program package.³⁹ The resolution-of-identity (RI) approximation was applied in all calculations.^{36,40} A self-consistent-field convergence threshold of 10^{−8} Hartree and geometry convergence thresholds of 10^{−8} Hartree and 10^{−5} Hartree Bohr^{−1} for the total energy and the Cartesian gradient, respectively, were used. The numerical quadrature was performed on TURBOMOLE's grid 5. All energy differences were corrected for harmonic zero-point vibrational energies.

These computations do not include spin-orbit coupling effects, nor do they allow for a direct assessment of the Stark splitting of the europium energy levels by the ligand field. The computation of the transition energies is described in the following section.

Ligand-field computations

Ligand field theory is at present the only practical model to analyze and simulate the level structures of lanthanoid ions in crystal hosts at an accuracy level of about 50 cm^{−1}.^{19,43–48} In the present work, the theoretical interpretation of the spectra was achieved using McPHASE's^{41,42} implementation of ligand-field theory using the F^k and ζ parameters optimized for the nonanuclear [Eu₉(PLN)₁₆(OH)₁₀]⁺ complex.¹¹

The McPHASE⁴² *pointc* module was used to calculate the relevant real-valued Wybourne normalized ligand-field parameters

(L_{kp} , Appendix D.4 in ref. 42) from the natural population analysis⁴⁹ point charges computed at the RI-B-P/def2-TZVPP level of theory. As the Eu(III) point charges were found to differ from the expected charge (+3), the Eu(III) point charge was increased to +3, the alkaline earth dication point charge was increased to +2, and the compensating oxygen point charges were scaled correspondingly to retain a total charge of +1 for the whole complex (*cf.* ref. 4). The Stark splitting of the ⁷F₂ level resulting from this ligand field as well as the related transition energies was then evaluated using the *iclion* module of McPHASE. The values of the F^k and ζ parameters used in the present work and optimized for the nonanuclear complex [Eu₉(PLN)₁₆(OH)₁₀]⁺ (constrained optimization)¹¹ are transferable to other Eu(III) complexes as illustrated both by the present work and for the [Eu(PLN)₃A]⁺ complexes with A = Li, Na, K, Rb, and Cs (see the ESI of ref. 11).

Symmetry assessment

In order to quantify the distortion of the coordination site with respect to idealized polyhedra for six-fold coordinated Eu(III) ions, we made use of the shape analysis method as defined in ref. 50. The ligand atoms coordinating the lanthanoid form the vertices of a polyhedron whose m dihedral angles along the edges, A_i defined as the angles between the normals of adjacent faces of the polyhedron, can be compared to the dihedral angles, B_i , of ideal polyhedra. The degree of distortion from an ideal case is evaluated by determining the “shape measure”

$$S = \min \left[\sqrt{\frac{1}{m} \sum_{i=1}^m (A_i - B_i)^2} \right] \quad (3)$$

which is the minimal (all possible superpositions considered) mean deviation of the dihedral angles along all edges. The smallest S value corresponds to the ideal polyhedron most suitable for describing the actual symmetry of the complex.

The figures of the computed structures were generated using Platon.⁵¹

Results

Computed structures

Geometry optimizations yielded four possible motifs for all three alkaline earth dications investigated (motifs 1, 2, 3, and 4 in Fig. 2 and enlarged in the ESI-1†). Motifs 1 and 2 correspond to six-fold coordinated Eu(III) ions and five-fold coordinated alkaline earth ions, while motifs 3 and 4 correspond to four-fold coordinated alkaline earth ions and six-/seven-fold coordinated Eu(III) ions, respectively.

Motif 1 corresponds to structures where one PLN unit coordinates with solely the Eu(III) ion, while the other three are bridging ligands between the Eu(III) ion and the alkaline earth ion. The tilt of the non-bridging ligand with respect to the europium-alkaline earth atom line slightly decreases (from 27° (Mg) to 23° (Sr)).

In motif 2, three ligands form a propeller-like unit centered on the Eu(III) ion, similar to those found for the [Eu(PLN)₃A]⁺

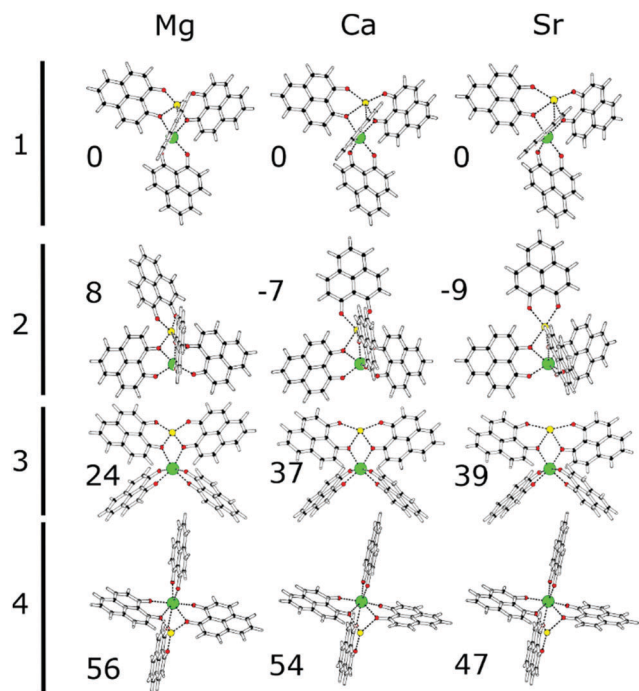


Fig. 2 Structures computed at the RI-B-P/def2-TZVPP level. Motif 2 has the lowest energy except for the species containing magnesium. Energy differences at the RI-B-P/def2-TZVPP level given in kJ mol^{-1} , including harmonic zero-point vibrational corrections. Eu atoms are represented in green, AE in yellow, and oxygen atoms in red. Enlarged as Fig. SI-1 (ESI[†]).

species,⁴ while the fourth one only coordinates with the alkaline earth ion sitting on top of the propeller along its symmetry axis. The alkaline earth coordinating ligand is tilted with respect to the Eu–AE atom line in the Mg containing complex (14°), while the same tilt angle in the Ca and Sr containing species is smaller ($\sim 4\text{--}5^\circ$). The propeller subunits are very similar with only the Mg containing complex showing a small deviation from the three-fold symmetry. Motif 2 structures are lower in energy by 7–9 kJ mol^{-1} at the RI-B-P/def2-TZVPP level except for $[\text{Eu}(\text{PLN})_4\text{Mg}]^+$, where the motif 1 structure is found to be lower in energy by 8 kJ mol^{-1} . These very small energy differences (making the two motifs practically isoenergetic) are also supported by B2PLYP/def2-TZVPP⁵² single point computations at the respective geometries (the energy differences amount to +1, –12, and –11 kJ mol^{-1} for Mg, Ca, and Sr containing structures, respectively; for the MP2 part of the computations the auxiliary basis functions described in ref. 38, 53 and 54 were used).

The Eu–alkaline earth distances increase with the ionic radius of the metal as one would expect. The distances are about 1% larger in motif 2 (322–375 pm) than in motif 1 (318–372 pm). The Eu–oxygen distances in the oxygen coordination sphere however are the same for all complexes (ranging from 223 to 246 pm, with an average of 234–236 pm). To further check the suitability of the employed BP functional, we also performed geometry optimizations and the subsequent ligand field computations of motif 1 and motif 2 structures using the B3LYP functional^{35,55,56} augmented with the D3 dispersion correction⁵⁷ employing Becke and Johnson damping.⁵⁸ The results do not differ

significantly from those obtained employing the BP functional and are provided in Fig. SI-2 of the ESI[†], as well as the corresponding xyz coordinates.

Motif 3 is a higher energy motif corresponding to more open structures where two PLN units coordinate only with the Eu(III) ion, while the other two are bridging ligands between the europium and alkaline earth ions.

Motif 4 is an even higher energy motif corresponding to cross-shaped structures where one PLN unit coordinates only with the Eu(III) ion, two ligands serve as bridging ligands, while the fourth one mainly but not exclusively coordinates with the alkaline earth ion.

The local coordination symmetry of the Eu(III) ion is provided *via* an estimate of the degree of distortion from ideal 6-coordination polyhedra using the “shape measure” criterion S .⁵⁰ The ideal polyhedra relevant to the present work are an octahedron (O_h) and a trigonal prism (D_{3h}), as defined in ref. 59. In our shape measure calculations we consider only the oxygen atoms around the Eu(III) ion. The results of the analysis are presented in Table 1, small values of S indicate coordination sites approaching the corresponding ideal polyhedra.

The results in Table 1 allow ordering the structures systematically: motif 1 complexes are closer to an octahedral configuration, which becomes more pronounced as the size of the alkaline earth ion increases. At least in the case of Ca and Sr, it is appropriate to call the coordination a distorted octahedron. In contrast, motif 2 complexes are distorted trigonal prisms. The octahedral character of motif 2 is weak, however it also increases with the increasing size of the alkaline earth ion. The motif 3 coordination site can be described as approaching O_h , while motif 4 strongly deviates from both O_h and D_{3h} as can be expected from a seven-fold coordinated site.

Trapped ion mobility

The results of the trapped ion mobility measurements are displayed in Fig. 3. Several isomers are observed in all three cases (Mg, Ca, and Sr).

Comparing the computed cross-sections listed in Table 2 with those extracted from the measurements – and assuming (systematic) deviations between experiment and computations less than or equal to 2 \AA^2 – the following assignments are possible:

(a) $[\text{Eu}(\text{PLN})_4\text{Mg}]^+$: at the achieved resolution, at least two different isomers are observed. The slightly less abundant peak with a cross-section of 301.6 \AA^2 can be assigned to motif 3, while the dominating peak with a cross-section of 305.6 \AA^2 is consistent with motifs 1, 2, and 4;

Table 1 Calculated shape measure criteria for all the complexes

/ $^\circ$	Motif 1		Motif 2		Motif 3		Motif 4 ^a	
	$S(O_h)$	$S(D_{3h})$	$S(O_h)$	$S(D_{3h})$	$S(O_h)$	$S(D_{3h})$	$S(O_h)$	$S(D_{3h})$
Mg	21	27	44	5	14	33	41	43
Ca	15	34	38	8	13	35	40	43
Sr	12	37	33	12	12	36	40	43

^a The symmetry analysis does not correctly apply to motif 4 since it has a 7-fold coordination symmetry.

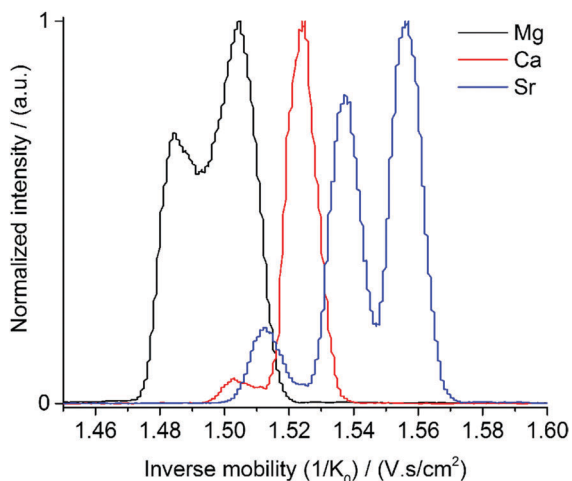


Fig. 3 Mobilograms of the $[\text{Eu}(\text{PLN})_4\text{AE}]^+$ coordination complexes with $\text{AE} = \text{Mg}, \text{Ca},$ and Sr plotted as ion intensity versus inverse mobility and obtained using trapped ion mobility spectroscopy (TIMS). The TIMS resolutions are (109, 81) for Mg, (112, 137) for Ca, and (130, 134, 135) for Sr peaks.

Table 2 Comparison of the measured and computed cross-sections for all the complexes

Exp. (\AA^2)	Motif 1 (\AA^2)	Motif 2 (\AA^2)	Motif 3 (\AA^2)	Motif 4 (\AA^2)
Mg 301.6/305.6	307.0	306.4	301.0	307.0
Ca 305.3/309.6	307.8	312.3	301.0	307.9
Sr 307.0/312.0/ 315.9	308.2	315.0	301.2	307.9

(b) $[\text{Eu}(\text{PLN})_4\text{Ca}]^+$: the cross-section of the dominant peak is consistent with motif 2, while the minor peak corresponds to motif 1 and/or motif 4;

(c) $[\text{Eu}(\text{PLN})_4\text{Sr}]^+$: three different peaks are experimentally resolved. The most abundant is again consistent with motif 2, while the least abundant is consistent with motifs 1 and 4. The intermediate peak remains to be assigned.

Due to the similarity of some of the calculated cross-sections and the associated uncertainties, a unique assignment of all

the peaks of Fig. 3 is currently not possible. It is however apparent that the species dominating the TIMS spectra are those with the largest cross-section and that their cross-sections match those of the motif 2 isomer family best. Only in the $[\text{Eu}(\text{PLN})_4\text{Mg}]^+$ case the TIMS data does not rule out contributions from motifs 1 and 4 to the dominant peak.

Gas-phase luminescence spectra

$[\text{Eu}(\text{PLN})_4\text{AE}]^+$ with $\text{AE} = \text{Mg}, \text{Ca},$ and Sr luminesce in the gas phase upon excitation at 458 nm (Fig. 4). These complexes show some of the characteristic narrow emission bands of the $\text{Eu}(\text{III})$ ion corresponding to the $^5\text{D}_0 \rightarrow ^7\text{F}_J$ transitions with $J = 2, 3,$ and 4. The $^5\text{D}_0 \rightarrow ^7\text{F}_{J=0,1}$ lines are either not observed or very weak (see Fig. SI-3, ESI† for a spectrum acquired at higher irradiance and lower resolution leading to a better signal to noise ratio).

The dominating $^5\text{D}_0 \rightarrow ^7\text{F}_2$ hypersensitive bands of each $\text{Eu}(\text{PLN})_4\text{AE}^+$ (about 620 nm) are split into two components. These components display a systematic trend with the alkaline earth ion radius characterizing the studied species (Fig. 5) similar to the case of the alkali adducts, $[\text{Eu}(\text{PLN})_3\text{A}]^+$ with $\text{A} = \text{Li}, \text{Na}, \text{K}, \text{Rb},$ and Cs reported in ref. 4.

The very low probability of the system to undergo a $^5\text{D}_0 \rightarrow ^7\text{F}_0$ transition may be explained by the symmetry of the $\text{Eu}(\text{III})$ coordination site as discussed later, while the magnetic dipole allowed $^5\text{D}_0 \rightarrow ^7\text{F}_1$ band (see Fig. 4 and Fig. SI-3, ESI†) is too weak to be analyzed. The following discussion therefore focuses on the hypersensitive band as in the case of ref. 4.

The results of the ligand-field computations for the $^5\text{D}_0 \rightarrow ^7\text{F}_2$ band are presented in Fig. 6b, c and Fig. SI-4b–e (ESI†). To facilitate comparison with the experiment, we summarize the experimental data in terms of a contour map showing transition energies and relative intensities together (Fig. 6a and Fig. SI-4a, ESI†). We assume identical amplitudes for the transitions belonging to the $^5\text{D}_0 \rightarrow ^7\text{F}_2$ band as intensities are currently not accessible, and mimic the experimental broadening with appropriately scaled Gaussian functions, whose width corresponds to the experimental resolution and whose superposition yields the maxima displayed. It is noteworthy that the experimental linewidths of the high

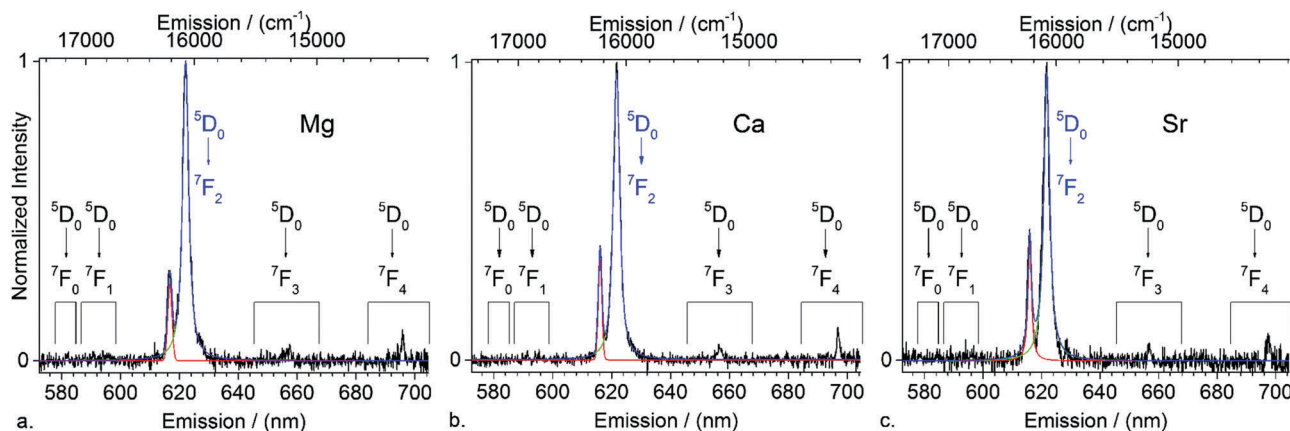


Fig. 4 Spectra of (a) $[\text{Eu}(\text{PLN})_4\text{Mg}]^+$, (b) $[\text{Eu}(\text{PLN})_4\text{Ca}]^+$, and (c) $[\text{Eu}(\text{PLN})_4\text{Sr}]^+$ recorded at 85K under 780 W cm^{-2} excitation at 458 nm and a ~ 0.2 mbar He buffer gas pressure. The spectral resolution is 0.7 nm. Accumulation time 12 000 s. The $^5\text{D}_0 \rightarrow ^7\text{F}_2$ hypersensitive band fitting involved two Voigt profiles (red and green).

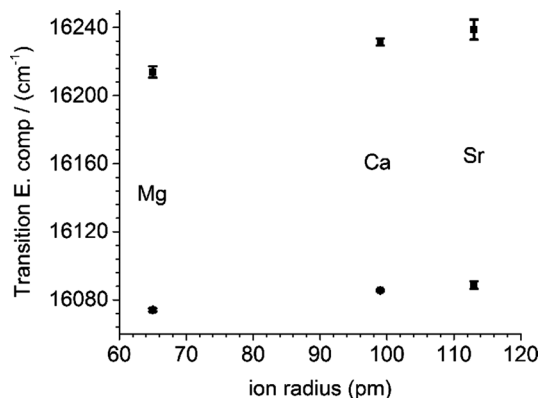


Fig. 5 Energies of the upper and lower components of the ${}^5D_0 \rightarrow {}^7F_2$ emission band of the $[\text{Eu}(\text{PLN})_4\text{AE}]^+$ complexes as a function of the ionic radius of the alkaline earth ion (AE = Mg, Ca, and Sr).

and low energy components evolve from (1.72, 2.55) nm for Mg, (1.47, 2.68) nm for Ca, and (1.45, 2.43) nm for Sr, respectively. The variation of the experimental linewidth is consistent with the existence of a third unresolved intermediate energy component – expected for the coordination site symmetries investigated here – as well as with the superposition of the contributions of different isomers.

From Fig. SI-4 (ESI[†]), it is obvious that motifs 3 and 4 do not match the observed splitting in terms of the number and position of sublevels. If one considers only the Ca and Sr adducts, motifs 1 and 2 reproduce the observed ${}^5D_0 \rightarrow {}^7F_2$ transitions equally well. The spectra computed for motifs 1 and 2 do however significantly differ for the $[\text{Eu}(\text{PLN})_4\text{Mg}]^+$ species. In that case, the two components of motif 2 agree significantly better with the experimental results than motif 1. Admittedly, to decide between motifs 1 and 2 one would need accurate computed intensities. A superposition of the different motifs with the experimental data is provided as Fig. SI-6 (ESI[†]).

Discussion

A comparison of the experimental results with the computed photoluminescence spectra and collision cross-sections leads

us to conclude that contributions of motif 3 and 4 isomers appear to be negligible.

The experimental data point instead towards motif 1 and/or motif 2 being the main contributors to the observed photoluminescence. Under the assumption that only one structural family significantly contributes to the observed photoluminescence, only motif 2 remains. This interpretation is in agreement with the computed relative energies (Fig. 2): motif 1 and 2 isomers are isoenergetic within the expected computational uncertainties, while motifs 3 and 4 are significantly higher in energy ($>20 \text{ kJ mol}^{-1}$).

The TIMS measurements show that motif 2 isomers are the dominant species for Ca and Sr. In the Mg case, the computed cross-sections do not allow us to decide between motifs 1, 2 and 4. Besides the issue of unknown differences in photoluminescence brightness between the different motifs, it is worth mentioning that the isomer populations might be slightly different in the gas-phase luminescence and ion mobility experiments due to the different ion source conditions pertaining.

In short, we cannot exclude that several structural motifs contribute to the measured photoluminescence spectra. Nevertheless, if we assume that only one structural motif contributes significantly to the observed photoluminescence, these brightest $[\text{Eu}(\text{PLN})_4\text{AE}]^+$ ions are best described as consisting of a neutral propeller subunit, $\text{Eu}(\text{PLN})_3$, with a six-fold europium coordination site attached to a $[\text{AE}(\text{PLN})]^+$ monocation (motif 2). The observed Stark splitting of the 7F_2 level is also consistent with the near D_{3h} trigonal prismatic configuration of the oxygen atoms of motif 2, while this arrangement is also consistent with the absence of the detectable ${}^5D_0 \rightarrow {}^7F_0$ transition which is forbidden under both D_{3h} and D_3 symmetries.²⁰ The linewidth trend of the components of the ${}^5D_0 \rightarrow {}^7F_2$ hypersensitive band can subsequently be explained by a small distortion caused by the presence of the alkaline earth dications: with the ligand field being effectively C_3 (approaching D_3), the ${}^5D_0 \rightarrow {}^7F_2$ hypersensitive band is expected to display, resolution allowing, three components instead of two for a D_3 (approaching D_{3h}) coordination site.²⁰

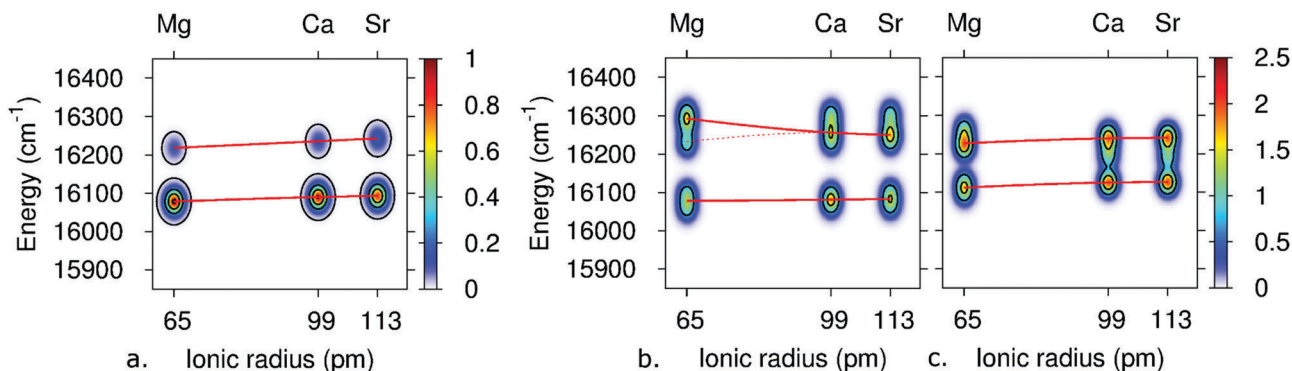


Fig. 6 (a) Experimental band positions and relative intensities for the ${}^5D_0 \rightarrow {}^7F_2$ transitions of $[\text{Eu}(\text{PLN})_4\text{AE}]^+$ with AE = Mg, Ca, and Sr. (b and c) Computed transitions from the 5D_0 level to the split 7F_2 level manifolds calculated using McPHASE for the motif 1 (b) and motif 2 (c) geometries (see text). Red lines are used to highlight the trends. The absolute values of the computed transitions are given in the ESI[†]. Motifs 3 and 4 are provided in the ESI[†]; see Fig. SI-4. For the sake of comparison, the corresponding contour plots for the BH-LYP-D3/def2-TZVPP geometries of motifs 1 and 2 are provided in Fig. SI-5 (ESI[†]).

Conclusions

The photoluminescence measurements of the mass-selected $[\text{Eu}(\text{PLN})_4\text{AE}]^+$ species (AE = Mg, Ca, and Sr) show a two-fold split of the $^5\text{D}_0 \rightarrow ^7\text{F}_2$ hypersensitive band. A weak blue shift is observed for both energy components of the $^5\text{D}_0 \rightarrow ^7\text{F}_2$ band when changing the adduct dication from Mg to Ca and from Ca to Sr, thereby similar to the trend observed for the alkali ions adducts of small ionic radius.⁴ The trends observed are best explained by the ligand fields of structures consisting of a six-fold coordinated Eu(III) ion part of a neutral propeller-like chelate, $\text{Eu}(\text{PLN})_3$, attached to a positively charged $[\text{AE}(\text{PLN})]^+$ subunit. Based on shape factor analysis, the Eu(III) coordination site is then close to trigonal prismatic. Compared to our previous study of the alkali complexes,⁴ the computed transition energies are now accurate to within about 50 cm^{-1} using the Slater integrals, F^k , and spin-orbit parameter, ζ , derived from the fitting procedure applied to the $[\text{Eu}_9(\text{PLN})_{16}(\text{OH})_{10}]^+$ complex.^{10,11} Nevertheless, our current spectral resolution and sensitivity do not allow us to completely rule out that more than one isomer family contributes to the observed photoluminescence.

We have demonstrated that trapped ion mobility analysis provides valuable information regarding the interpretation of gas-phase photoluminescence measurements. However, a unique one-to-one correlation between the experimentally inferred cross-sections and the computed structures is not always possible in the present case. This is due to the computed cross-sections being essentially identical for some of the candidate structures and the uncertainties affecting them. While the isomer populations might be slightly different in the gas-phase luminescence and ion mobility spectra due to different source conditions, the high resolution achieved in the TIMS measurements shown here highlights the next technical challenge for gas-phase photoluminescence measurements (on complex molecular ions): prior to the isolation of homogeneous ensembles of structural isomers.

A way to achieve this and thus to resolve potentially overlapping spectral contributions from different isomers would be to couple a trapped ion mobility cell to a trapped ion photoluminescence setup. Such coupling of ion mobility pre-selection with subsequent spectroscopy has so far only been realized in the context of (multi-)photon dissociation^{60–68} and photoelectron^{69–75} spectroscopies (albeit at lower ion mobility resolutions than those now accessible using TIMS).

Acknowledgements

This work has been supported by the Deutsche Forschungsgemeinschaft (DFG) through CRC/TRR 88 “Cooperative Effects in Homo- and Hetero-Metallic Complexes (3MET)” (Projects C1, C5, and C7). J.-F. G. acknowledges support from the Hector Fellow Academy (HFA). Some of the large-scale DFT computations presented in this work were performed on the computational resource InstitutsCluster II operated by the information technology center of the Karlsruhe Institute of Technology (KIT) and supported by the DFG. We also acknowledge the Bundesministerium für Bildung und Forschung (BMBF) through the Helmholtz

Research Program POF Science and Technology of Nano-systems for support and for providing the necessary infrastructure.

Notes and references

- 1 K. Binnemans, *Coord. Chem. Rev.*, 2015, **295**, 1–45.
- 2 J. C. G. Bünzli, *Coord. Chem. Rev.*, 2015, **293–294**, 19–47.
- 3 S. V. Eliseeva and J. C. G. Bünzli, *Chem. Soc. Rev.*, 2010, **39**, 189–227.
- 4 J. F. Greisch, M. E. Harding, B. Schäfer, M. Rotter, M. Ruben, W. Klopfer, M. M. Kappes and D. Schooss, *J. Phys. Chem. A*, 2014, **118**, 94–102.
- 5 R. V. Smith, P. W. Erhardt, D. B. Rusterholtz and C. F. Barfknecht, *J. Pharm. Sci.*, 1976, **65**, 412–417.
- 6 R. Hazama, K. Umakoshi, C. Kabuto, K. Kabuto and Y. Sasaki, *Chem. Commun.*, 1996, 15–16.
- 7 W. P. Grygiel and M. E. Starzak, *Biophys. Chem.*, 1996, **60**, 39–44.
- 8 W. G. Gonzalez, V. Ramos, M. Diaz, A. Garabedian, J. C. Molano-Arevalo, F. Fernandez-Lima and J. Miksovská, *Biochemistry*, 2016, **55**, 1873–1886.
- 9 W. P. Grygiel and M. E. Starzak, *Biophys. Chem.*, 1996, **60**, 39–44.
- 10 J. F. Greisch, M. E. Harding, B. Schäfer, M. Ruben, W. Klopfer, M. M. Kappes and D. Schooss, *J. Phys. Chem. Lett.*, 2014, **5**, 1727–1731.
- 11 J. F. Greisch, J. Chmela, M. E. Harding, W. Klopfer, M. M. Kappes and D. Schooss, *Inorg. Chem.*, 2016, **55**, 3316–3323.
- 12 F. A. Fernandez-Lima, D. A. Kaplan and M. A. Park, *Rev. Sci. Instrum.*, 2011, **82**, 126106.
- 13 F. A. Fernandez-Lima, D. A. Kaplan, J. Suetering and M. A. Park, *Int. J. Ion Mobility Spectrom.*, 2011, **14**, 93–98.
- 14 D. A. Hernandez, J. D. DeBord, M. E. Ridgeway, D. A. Kaplan, M. A. Park and F. Fernandez-Lima, *Analyst*, 2014, **139**, 1913–1921.
- 15 T. D. Pasatoiu, A. M. Madalan, M. U. Kumke, C. Tiseanu and M. Andruh, *Inorg. Chem.*, 2010, **49**, 2310–2315.
- 16 D. Imbert, M. Cantuel, J. C. G. Bünzli, G. Bernardinelli and C. Piguet, *J. Am. Chem. Soc.*, 2003, **125**, 15698–15699.
- 17 R. van Deun, P. Fias, P. Nockemann, K. Van Hecke, L. Van Meervelt and K. Binnemans, *Inorg. Chem.*, 2006, **45**, 10416–10418.
- 18 R. van Deun, P. Nockemann, P. Fias, K. Van Hecke, L. Van Meervelt and K. Binnemans, *J. Chem. Soc., Chem. Commun.*, 2005, 590–592.
- 19 C. K. Duan and P. A. Tanner, *J. Phys. Chem. A*, 2010, **114**, 6055–6062.
- 20 P. A. Tanner, *Chem. Soc. Rev.*, 2013, **42**, 5090–5101.
- 21 M. P. Hehlen, M. G. Brik and K. W. Krämer, *J. Lumin.*, 2013, **136**, 221–239.
- 22 G. Blasse, *Inorg. Chim. Acta*, 1988, **142**, 153–154.
- 23 G. Vicentini, L. B. Zinner, J. Zuckerman-Schpector and K. Zinner, *Coord. Chem. Rev.*, 2000, **196**, 353–382.
- 24 J. C. G. Bünzli, N. André, M. Elhabiri, G. Muller and C. Piguet, *J. Alloys Compd.*, 2000, **303–304**, 66–74.

- 25 E. E. Castellano, G. Oliva, J. Zuckerman-Schpector, G. Vicentini and L. R. F. de Carvalho, *Inorg. Chim. Acta*, 1985, **109**, 33–37.
- 26 P. Benigni and F. Fernandez-Lima, *Anal. Chem.*, 2016, **88**, 7404–7412.
- 27 M. F. Mesleh, J. M. Hunter, A. A. Shvartsburg, G. C. Schatz and M. F. Jarrold, *J. Phys. Chem.*, 1996, **100**, 16082–16086.
- 28 A. A. Shvartsburg and M. F. Jarrold, *Chem. Phys. Lett.*, 1996, **261**, 86–91.
- 29 I. Campuzano, M. F. Bush, C. V. Robinson, C. Beaumont, K. Richardson, H. Kim and H. I. Kim, *Anal. Chem.*, 2012, **84**, 1026–1033.
- 30 M. F. Bush, I. Campuzano and C. V. Robinson, *Anal. Chem.*, 2012, **84**, 7124–7130.
- 31 M. Kordel, D. Schooss, C. Neiss, L. Walter and M. M. Kappes, *J. Phys. Chem. A*, 2010, **114**, 5509–5514.
- 32 R. O. Freire and A. M. Simas, *J. Chem. Theory Comput.*, 2010, **6**, 2019–2023.
- 33 J. J. P. Stewart, *MOPAC2012*, Stewart Computational Chemistry, Colorado Springs, CO, USA, 2012, [HTTP://OpenMOPAC.net](http://OpenMOPAC.net).
- 34 J. J. P. Stewart, *J. Mol. Model.*, 2013, **19**, 1–32.
- 35 A. D. Becke, *Phys. Rev. A: At., Mol., Opt. Phys.*, 1988, **38**, 3098–3100.
- 36 R. Gulde, P. Pollak and F. Weigend, *J. Chem. Theory Comput.*, 2012, **8**, 4062–4068.
- 37 F. Weigend and R. Ahlrichs, *Phys. Chem. Chem. Phys.*, 2005, **7**, 3297–3305.
- 38 F. Weigend, M. Häser, H. Patzelt and R. Ahlrichs, *Chem. Phys. Lett.*, 1998, **294**, 143–152.
- 39 TURBOMOLE V6.4 2012, a development of University of Karlsruhe and Forschungszentrum Karlsruhe GmbH, 1989–2007, TURBOMOLE GmbH, since 2007, available from <http://www.turbomole.com>.
- 40 F. Weigend, *Phys. Chem. Chem. Phys.*, 2006, **8**, 1057–1065.
- 41 M. Rotter, *J. Magn. Magn. Mater.*, 2004, **272–276**, E481–E482.
- 42 M. Rotter, M. Duc Le, A. T. Boothroyd and J. A. Blanco, *J. Phys.: Condens. Matter*, 2012, **24**, 213201.
- 43 C. Holzer, A. M. Wernbacher, J. M. Senekowitsch, K. Gatterer and A. M. Kelterer, *J. Phys. Chem. A*, 2014, **118**, 11499–11511.
- 44 W. T. Carnall, G. L. Goodman, K. Rajnak and R. S. Rana, *J. Chem. Phys.*, 1989, **90**, 3443–3457.
- 45 D. J. Newman, *Adv. Phys.*, 1971, **20**, 197–256.
- 46 K. Rajnak and B. G. Wybourne, *Phys. Rev.*, 1963, **132**, 280–290.
- 47 K. Rajnak and B. G. Wybourne, *J. Chem. Phys.*, 1964, **41**, 565–569.
- 48 G. Racah, *Phys. Rev.*, 1949, **76**, 1352–1365.
- 49 A. E. Reed, R. B. Weinstock and F. Weinhold, *J. Chem. Phys.*, 1985, **83**, 735–746.
- 50 J. Xu, D. G. Churchill, M. Botta and K. N. Raymond, *Inorg. Chem.*, 2004, **43**, 5492–5494.
- 51 A. L. Spek, *Acta Crystallogr.*, 2009, **D65**, 148–155.
- 52 S. Grimme, *J. Chem. Phys.*, 2006, **124**, 034108.
- 53 A. Hellweg, C. Hättig, S. Höfener and W. Klopper, *Theor. Chem. Acc.*, 2007, **117**, 587–597.
- 54 J. Chmela, PhD thesis, Karlsruhe Institute of Technology, 2016.
- 55 C. Lee, W. Yang and R. G. Parr, *Phys. Rev. [Sect.] B*, 1988, **37**, 785–789.
- 56 A. D. Becke, *J. Chem. Phys.*, 1993, **98**, 1372–1377.
- 57 S. Grimme, J. Antony, S. Ehrlich and H. Krieg, *J. Chem. Phys.*, 2010, **132**, 154104.
- 58 S. Grimme, S. Ehrlich and L. Goerigk, *J. Comput. Chem.*, 2011, **32**, 1456–1465.
- 59 E. L. Muettterties and L. J. Guggenberger, *J. Am. Chem. Soc.*, 1974, **96**, 1748–1756.
- 60 G. Papadopoulos, A. Svendsen, O. V. Boyarkin and T. R. Rizzo, *Faraday Discuss.*, 2011, **150**, 243–255.
- 61 L. Voronina and T. R. Rizzo, *Phys. Chem. Chem. Phys.*, 2015, **17**, 25828–25836.
- 62 A. Masson, M. Z. Kamrath, M. A. S. Perez, M. S. Glover, U. Rothlisberger, D. E. Clemmer and T. R. Rizzo, *J. Am. Soc. Mass Spectrom.*, 2015, **26**, 1444–1454.
- 63 L. Voronina, A. Masson, M. Z. Kamrath, F. Schubert, D. E. Clemmer, C. Baldauf and T. R. Rizzo, *J. Am. Soc. Mass Spectrom.*, 2016, **138**, 9224–9233.
- 64 B. D. Adamson, N. J. A. Coughlan, P. B. Markworth, R. E. Continetti and E. J. Bieske, *Rev. Sci. Instrum.*, 2014, **85**, 123109.
- 65 A. Theisen, B. Yan, J. M. Brown, M. Morris, B. Bellina and P. E. Barran, *Anal. Chem.*, 2016, **88**, 9964–9971.
- 66 B. D. Adamson, N. J. A. Coughlan, R. E. Continetti and E. J. Bieske, *Phys. Chem. Chem. Phys.*, 2013, **15**, 9540–9548.
- 67 N. J. A. Coughlan, B. D. Adamson, K. J. Catani, U. Wille and E. J. Bieske, *J. Phys. Chem. Lett.*, 2014, **5**, 3195–3199.
- 68 O. Hernandez, S. Isenberg, V. Steinmetz, G. L. Glish and P. Maître, *J. Phys. Chem. A*, 2015, **119**, 6057–6064.
- 69 R. Fromhertz, G. Ganteför and A. A. Shvartsburg, *Phys. Rev. Lett.*, 2002, **89**, 083001.
- 70 J. C. Pouilly, F. Lecomte, N. Nieuwjaer, B. Manil, J. P. Schermann, C. Desfrancois, G. Grégoire, R. Ballivian, F. Chirot, J. Lemoine, F. Calvo, R. Antoine and P. Dugourd, *Int. J. Mass Spectrom.*, 2010, **297**, 28–35.
- 71 M. Vonderach, O. T. Ehrler, K. Matheis, T. Karspuschkin, E. Papalazarou, C. Brunet, R. Antoine, P. Weis, O. Hampe, M. M. Kappes and P. Dugourd, *Phys. Chem. Chem. Phys.*, 2011, **13**, 15554–15558.
- 72 M. Vonderach, O. T. Ehrler, P. Weis and M. M. Kappes, *Anal. Chem.*, 2011, **83**, 1108–1115.
- 73 M. Vonderach, M. O. Winghart, L. MacAleese, F. Chirot, R. Antoine, P. Dugourd, P. Weis, O. Hampe and M. M. Kappes, *Phys. Chem. Chem. Phys.*, 2014, **16**, 3007–3013.
- 74 M. Vonderach, O. T. Ehrler, K. Matheis, P. Weis and M. M. Kappes, *J. Am. Chem. Soc.*, 2012, **134**, 7830–7841.
- 75 U. Schwarz, M. Vonderach, M. K. Armbruster, K. Fink, M. M. Kappes and P. Weis, *J. Phys. Chem. A*, 2014, **118**, 369–379.